Front. Earth Sci. 2015, 9(3): 412–426
DOI 10.1007/s11707-014-0481-4

RESEARCH ARTICLE

Influence of pore pressure on tensile fracture growth in rocks: a new explanation based on numerical testing

Shou MA (✉)[1,2], Jianchun GUO[1], Lianchong LI[3], Leslie George THAM[4], Yingjie XIA[3], Chun'an TANG[3]

1 State Key Laboratory of Oil and Gas Geology and Exploitation, Southwest Petroleum University, Chengdu 610500, China
2 SINOPEC Shengli Oilfield Company, Dongying 257000, China
3 School of Civil Engineering, Dalian University of Technology, Dalian 116024, China
4 Department of Civil Engineering, The University of Hong Kong, Hong Kong, China

Abstract The diffusion of pore fluid pressures may create both spatial and temporal effective stress gradients that influence or control the development and evolution of fractures within rock masses. To better understand the controls on fracturing behavior, numerical simulations are performed using a progressive fracture modeling approach that shares many of the same natural kinematic features in rocks, such as fracture growth, nucleation, and termination. First, the pinch-off breaking test is numerically performed to investigate the tensile failure of a rock specimen in a uniform pore pressure field. In this numerical simulation, both mechanical and hydrological properties of a suite of rocks are measured under simulated laboratory conditions. The complete tensional failure process of the rock specimen under pore pressure was reproduced. Second, a double-notched specimen is numerically extended to investigate how the water flow direction or pore pressure gradient influences the fracture growth. An exhaustive sensitivity study is conducted that examines the effects of varying both hydrological and mechanical boundary conditions. The simulation results indicate that local fluid pressure gradients strongly influence the state of stress in the solids and, thereby, fracture growth. Fracture and strength behavior is influenced not only by the pore pressure magnitude on a local scale around the fracture tip, but also by the orientation and distribution of pore pressure gradients on a global scale. Increasing the fracture growth rate increases the local model permeability and decreases the sample strength. The results of this study may provide useful information concerning the degree of hydrological and mechanical coupling action under geologic conditions.

Received February 11, 2014; accepted July 14, 2014

E-mail: mashou_sinopec@163.com

Keywords pore pressure, effective stress, heterogeneous, numerical simulation, fracture growth, rock

1 Introduction

Within rock and civil engineering structures, general issues concerning fluid flow cannot be resolved in any practical manner prior to investigating the fracturing behavior of rocks under pore fluid pressure and the original nature of the fracture networks themselves. The diffusion of pore fluid pressures may create both spatial and temporal effective stress gradients that influence or control the development and evolution of fractures within rock masses.

Fluid-saturated rock failure may be studied by two different approaches. The first is based on linear elastic fracture mechanics, which has several attractive features, including the Griffith assumption of critical strain energy release rate (Griffith, 1920). Several researchers have applied this approach to study hydraulic fracture problems (Abou-Sayed et al., 1978; Rummel, 1987; Detournay et al., 1989; Bruno and Nakagawa 1991). Their investigations considered the effects of internal fracture fluid pressure on the fracture tip stress intensity factor and the contribution of pore pressure to the change in total potential energy necessary for fracture extension. The second is the material strength approach, in which the stress state is determined from elasticity equations and failure is assumed to occur when the conventional effective stress exceeds the strength of the rocks (Jaeger and Cook, 1963; Boone et al., 1986; Tang et al., 2002; Haeri et al., 2014b). This approach allows one to obtain the load level and the location in a structure where the rock first reaches failure. This point is assumed to be the location of initial fracturing or fracture growth.

Although both the fracture mechanics and material strength approaches provide a general understanding of fluid-driven fracture, analytical solutions are available for only a few simplified situations with the assumption of homogeneity (Jaeger and Cook 1979; Bruno and Nakagawa 1991; Wong et al., 2006; Shimizu et al., 2011; Pan et al., 2011). In fact, disregarding the heterogeneity, including mechanical and hydrological heterogeneity, of rocks could result in errors in the analysis of the hydraulic fracturing behavior.

First, the influence of the mechanical heterogeneity of rocks is very important in characterizing their fracturing behavior. It is well known that rock is a heterogeneous geological material made up of numerous types of natural weakness, such as pores, grain boundaries, and pre-existing cracks/fractures (Haeri et al., 2013; 2014a; Wu et al., 2013). When rock is subjected to hydraulic loading, these pre-existing defects can induce fracture or fracture growth, which can in turn change the structure of the rock and alter the fluid flow properties of the rock (Wang and Kemeny, 1994; Yang et al., 2004). These heterogeneity-related flow properties influence the hydraulic fracturing behavior in many ways. For example, the size of the micro-cracks or micro-fractures in the area of the rock surrounding the borehole or the initiated fracture tips, may increase. Consequently, a highly permeable damage zone or fracture growth zone is created around the fracture tip (Pan et al., 2011; 2014)

Second, a few researchers have investigated the influence of hydrological heterogeneity (e.g., a non-uniform or unsymmetrical pore pressure distribution) on fracture growth. In fact, many geological systems, such as magmatic dykes, mud volcanoes, hydrothermal vents, or fluid in faults, show evidence that pore pressure increase might be localized instead of being homogeneously distributed, or uniform, throughout the domain of interest (Jamveit et al., 2004). For example, some researchers studied the formation and expansion of fractures (including joints and large-scale faults) in the mid- to upper-crustal environment, where fluid pressure ranges between supra-lithostatic and hydrostatic, or even sub-hydrostatic (Holl et al., 1997; Oliver, 2001; Rozhko et al., 2007; Gudmundsson et al., 2012). In addition, the natural heterogeneousness of permeability can cause large pore pressure gradients on a certain spatial scale, and various man-made physical processes can cause the development of non-uniform pore pressure gradients in rock masses (Lin et al., 2014a, b). These processes include the development of large pore pressure gradients due to transients caused by the spatial heterogeneity of the expulsion of connate water during compaction, in situ sources of fluid pressures, and local gradients driving fluid diffusion. For example, hydraulic fracture in petroleum and geothermal engineering has been used to establish hydraulic communication between adjacent wellbores within a non-uniform pore pressure gradient. To design an efficient fractured line drive of production, one can establish an appropriate pore pressure gradient field before starting hydraulic fracturing operations to control the direction and growth of fractures (Bruno and Nakagawa, 1991; Kessels and Kuck, 1995; Berchenko and Detournay, 1997; Wangen, 2011).

Growing rock fractures generally tend to orient themselves parallel to the maximum compressive far-field stress, minimizing the energy required for extension. When the far-field stress state is more uniform, in situ stress effects may not dominate fracture orientation. In such situations, differences in pore pressure around the fracture tip can influence fracture direction on a local scale, while pressure gradient-induced body forces can affect fracture orientation on a more global scale. Little theoretical or empirical evidence has been presented to address these problems. In this study, numerical simulations using RFPA, a FEM-based code, are performed to investigate the influence of pore pressure on fracture growth in rocks. Although a reasonable number of numerical simulations using RFPA have been conducted in the modeling of the fracturing process associated with fluid flow (Tang et al., 2002; Li et al., 2011, 2012a, 2014), few simulations have been conducted to investigate the fracture growth of rocks in non-uniform pore pressure gradients. The simulated growth of fractures and their interactions, which are impossible to observe in the laboratory or field and are difficult to consider with static stress analysis approaches, may provide supplementary information on the stress distribution, failure-induced stress redistribution, pore pressure field evolution, and associated flow phenomena.

2 A brief introduction to the numerical code, RFPA

RFPA (Tang et al., 2002; Li et al., 2012b) represents a finite element code that can simulate the fracture and failure process of quasi-brittle materials such as rocks. To model rock, the rock sample (called the numerical specimen in RFPA modeling) is assumed to be composed of many mesoscopic elements, the material properties of which are different from one another and specified according to a Weibull distribution, as shown in Eq. (1) (Weibull, 1951).

$$f(u) = \frac{m}{u_0}\left(\frac{u}{u_0}\right)^{m-1} \exp\left(-\frac{u}{u_0}\right)^m, \qquad (1)$$

where u is the macroscopic magnitude of the parameters (such as Young's modulus, Poisson's ratio, strength properties, permeability, and heat conductivity), i.e., the real values obtained from laboratory tests, while the scale parameter u_0 is related to the average of the element parameter, i.e., the input values in numerical simulation. The homogeneity index m defines the shape of the distribution function and represents the degree of material

homogeneity. In general, it is assumed that the parameters of the element conform to individual distributions with the same heterogeneity index, which means all the parameters vary independently. A heterogeneous material can be produced numerically in a computer simulation for a material composed of many elements. Each element is assumed to be isotropic and homogeneous. Higher homogeneity indices lead to more homogeneous numerical samples.

In RFPA, the finite element method (FEM) is employed as the coupled fluid-solid analysis tool, where the four-node or eight-node isoparametric element is used as the basic element in the finite element mesh. For a more detailed introduction to RFPA, one can refer to the published papers of Tang et al. (2002) and Li et al. (2012b). In general, RFPA was developed under the following assumptions:

◆ The rock mass is assumed to be fully saturated with fluid flow governed by Darcy's law. Additionally, the coupled process between stress/strain and fluid flow in the deforming rock mass is governed by Biot's consolidation theory (Biot, 1941; Terzaghi, 1943).

◆ The rock material at the elemental scale is assumed to be elasto-brittle with a residual strength. The mechanical behavior of the element is described by an elastic damage constitutive law, and the residual strain/deformation upon unloading is not considered.

◆ An element is considered to fail in tensile mode when the minimum principal stress exceeds the tensile strength and in shear mode when the shear stress satisfies the Mohr–Coulomb failure criterion.

◆ The isotropic conditions are considered for the hydraulic behavior at the elemental scale, and the permeability of an element varies as a function of the stress state during elastic deformation and increases according to a deformation-dependent law when the element is damaged.

RFPA decomposes the stress field in a fractured rock into one of an elastic continuum and one of a fractured elastic body. The continuum damage principle is used to simulate the fracture growth, where the fractured rock is also assumed to be an equivalent continuous medium and the fracture is represented as the damaged zone. Strength heterogeneity was introduced by assigning different strength values to different sites, with stress heterogeneity being simulated by the introduction of a perturbation to the continuum stress field. Although the model was based on linear approximation, it can produce a nonlinear response (Blair and Cook, 1998; Tang et al., 2002; Renard et al., 2009). Unstable fracture growth is captured when a large area of damage occurs around the fracture tip in the rock sample or rock mass at a loading step. This approach to simulating fractures is similar to a smeared crack model (Malvar and Fourney, 1990; Pearce et al., 2000). Compared with a discrete crack model, calculations of the stress intensity factor and mesh rezoning are not needed in the proposed model. There is no need for a pre-existing fracture to simulate the fracture initiation and growth. With the advance in the performance of computers, an increasing number of researchers are attempting to use a similar principle to solve discontinuous problems through continuum mechanics (Yuan and Harrison, 2005; Pan et al., 2011, 2014).

3 Numerical verification of the effective stress law for tensile fracture in a uniform pore pressure field

The influence of pore pressure on brittle failure has been discussed by many researchers, expanding on Terzaghi's early experiments with soils and saturated concrete (Terzaghi, 1943). For quasi-static situations considering pore pressure, but in the absence of body forces, the stress equilibrium equations may be expressed as

$$\sigma_{ij}^{e} = \sigma_{ij} - \alpha p \delta_{ij} = 0, \tag{2}$$

in which σ_{ij}^{e} is the effective stress, p is the pore fluid pressure, σ_{ij} is total stress, δ_{ij} is the Kronecker delta (by convention, compressive stress is positive), and α is a constant (called as pore pressure coefficient). De Boer and Lade (1997) provide a summary of expressions for α, which is typically in the range of 0.80 to 0.95 for rocks. In terms of the equilibrium of effective stresses acting on the rock matrix, the pressure gradient term $-\alpha p \delta_{ij}$ is equivalent to body forces. A difference in pore pressure acting on two sides of a volume element of rock must be counteracted by a change in effective stress within the rock material in order to maintain force equilibrium.

It is difficult to quantitatively control the process of hydraulic fracture initiation and growth in laboratory tests, and it is also difficult to measure the global change of the pore pressure field due to fracture growth in heterogeneous rock. In this section, a 3D numerical test is first employed to verify the effective stress law for tensile fracture in a uniform pore pressure field. Bridgman (1912) conducted a pinch-off experiment in the laboratory to test the rupture of solids under hydrostatic pore pressure. As shown in Fig. 1(a), a rock specimen is placed in a vessel in the experiment. Radial seals are positioned near the ends of the rock specimen. Water is injected into the annular chamber between the specimen and the vessel inside the diameter at a known water pressure p. The ends of the specimen are open to the atmosphere so that fluid flows into the sample along the radial surface and then out each end. It is believed that fracture would initiate when the effective stress field satisfies the tensile failure criteria.

Based on the pinch-off experiment, a 3D model (Fig. 1(b)) is set up using RFPA. The dimensions of the model are 50 mm×50 mm×400 mm. The model is divided into a 50 mesh×50 mesh×400 mesh. The diameter of the rock

specimen is 25 mm. The physico-mechanical parameters of the rock specimen are listed in Table 1. Note that all of the simulations using RFPA operate on effective stresses. Mesh (grid) dependency is unavoidable in numerical modeling. Many studies have detailed the mesh effect (Zhu and Tang, 2004). These studies have shown that if the mesh size is too small, the computational resource will be wasted; in contrast, if the mesh size is too large, an evident calculation error will occur. To examine the associated mesh effect, two points are considered. One is to investigate the mesh effect associated with producing model results and the other is to identify the optimal mesh size with respect to the problem geometry. A size of 1 mesh/mm is employed when modeling a rock sample in the laboratory. It can be expected that this mesh size will meet the requirements of the calculation accuracy.

Before modeling the pinch-off experiment, the calibration of the mechanical parameters used in a Weibull statistical model should be conducted. In the modeling based on RFPA, the rock material is assumed to be heterogeneous. For a given homogeneity index m, there is a corresponding relation between the rock mass properties (macroscale parameters) and the numerical input parameters (meso-scale parameters), according to the Weibull distribution in Eq. (1). The homogeneity index should be determined according to the rock microstructure or the micro-defect size distribution (Liu et al., 2004; Wong et al., 2006). Due to the insufficient microstructure information in this study, yet sufficient macroscopic physical–mechanical parameters, a numerical simulation of a uniaxial compressive test is first conducted to fit the parameters. A group of parameters are pre-selected and input into the RFPA to calculate the uniaxial compressive strength, elastic modulus, and tensile strength, which are compared with the physico-mechanical properties observed in the experiment. If these values are consistent with each other, the input parameters are considered suitable.

The analysis and microstructural observations conducted by Wong et al. (2006) require the Weibull parameter m (i.e., the homogeneity index in this study) to be greater than 2.0, but to fall within the typical range of $m = 2.0-6.0$ as reported for engineering materials (McClintock and Argon, 1966). Using RFPA code, a series of numerical models with the same elemental seed parameters, but different homogeneity indices, was built to conduct a uniaxial compressive strength test. It is shown that the homogeneity index range of 1.2 to 5.0 is common for rock materials (Liu et al., 2004; Zhu and Tang 2004). Therefore, the Weibull parameter $m = 3.0$ is selected to describe the heterogeneous material properties of rock in this study. A numerical specimen with a width of 50 mm and a height of 100 mm is then defined. The specimen is

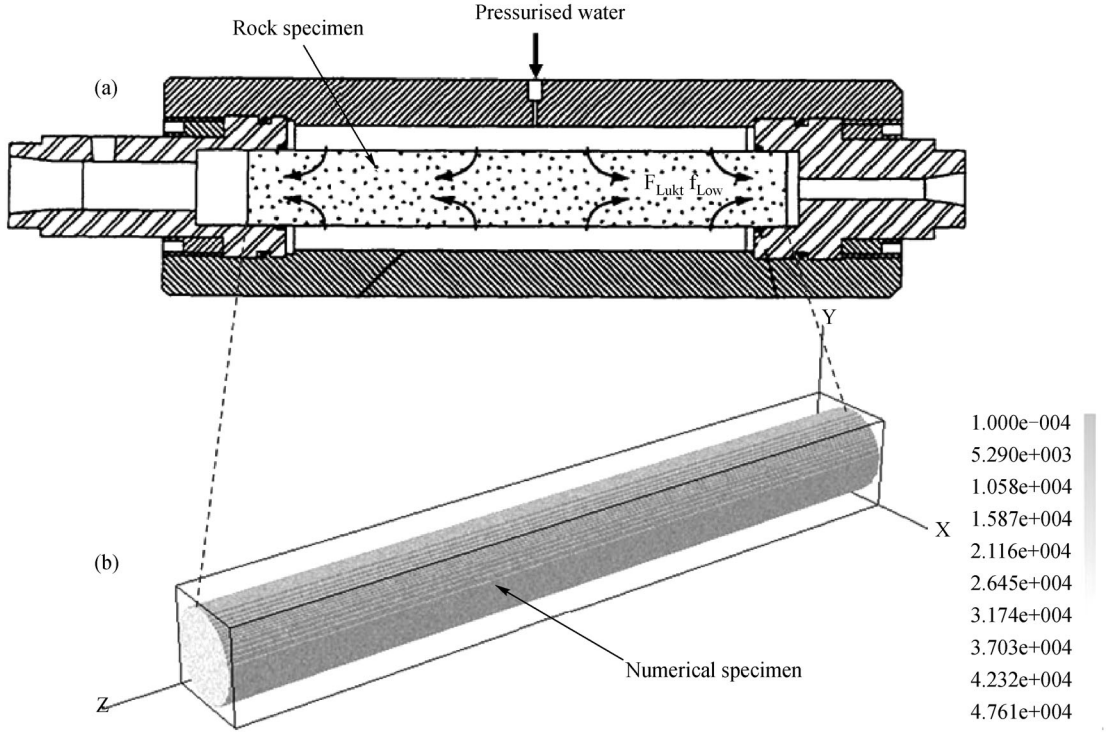

Fig. 1 Configuration for the pinch-off breaking experiment, (a) the experiment setup in the laboratory (Bruno and Nakagawa, 1991), and (b) the 3D numerical model represented with elastic modulus (the variance in the gray colors represent different values of the mechanical properties of the individual elements).

composed of 100 × 200 elements that are randomly produced by a computer according to the Weibull distribution for the given homogeneity index m = 3.0.

Previous studies (e.g., Tang et al., 2002; Liu et al., 2004; Zhu et al., 2006) have noted that the local heterogeneity greatly influences the mechanical responses, while the hydraulic responses are mainly determined by the newly developed fractures, i.e., the damage evolution and the macroscopic configuration of fractures. Hence, in this study, it is assumed that the Young's modulus and strength conform to two individual distributions with the same homogeneity index of 3.0, while the other parameters, including the Poisson's ratio, friction angle, and local permeability, are assumed to have a higher homogeneity index of 100.0.

An external displacement at a constant rate of 0.001 mm/step is then applied to the specimen in the axial direction. Figure 2 shows the results of the back analysis. The stress-strain relation for the specimen is given in Fig. 3. The elastic modulus and peak stress in the stress-strain curve are approximately 20 GPa and 80 MPa, respectively, which are consistent with the experimental data, i.e., the macroscopic magnitude of E and f_c in Eq. (1). In this model, the input heterogeneity index m, the mean value of Young's modulus E_0, the uniaxial compressive strength f_{c0}, and the tensile strength f_{t0} are 3.0, 25 GPa, 260 MPa, and 26 MPa, respectively. The main parameters involved in the following simulations are listed in Table 1.

Table 1 Physico-mechanical parameters used in numerical simulation

Parameter	Value
Homogeneity index (m)	3.0
Young's modulus – macroscopic value (E)*/GPa	20.0
Young's modulus (E_0) /GPa	25.0
Uniaxial compressive strength– macroscopic value (f_c)*/MPa	80.0
Uniaxial compressive strength (f_{c0})/MPa	260.0
Tensile strength– macroscopic value (f_t)*/MPa	8.0
Tensile strength (f_{t0})/MPa	26.0
Poisson's ratio (ν)	0.25
Friction angle (ϕ)/(°)	30
Permeability coefficient (k_0)/(m·day^{-1})	0.1
Coeff. of pore water pressure (α)	0.8
Damage factor of permeability (ξ)	100
Coupling coefficient (β)	0.01

*Young's modulus, uniaxial compressive strength and tensile strength are macroscopic values related to the experimental test in the laboratory.

With the calibration of the mechanical parameters used in the Weibull statistical model, the pinch-off experiment is modeled as follows. An increasing water pressure p with an increment of 0.1 MPa per step is applied to the radial surface of the model shown in Fig. 1(b). A constant pressure of 0.1 MPa is maintained at the left and right ends of the model. Therefore, the pore pressure within the model will be uniformly equal to p, except for the regions near the left and right ends of the rock core. The axisymmetric loading condition can ensure that no shear stresses act throughout the model. The problem is solved quasi-statically, i.e., the water flow is simulated as a steady process. Mathematically, the internal effective stresses over most of the specimen are, therefore:

$$\sigma_r^e = \sigma_\theta^e = (\alpha - 1)p, \tag{3}$$

$$\sigma_z^e = \alpha p, \tag{4}$$

i.e., the longitudinal effective stress in the specimen is tensile and equal to αp. With continued tensile loading (i.e., increases in pore pressure), the tensile strength of the intact rock specimen will be exceeded. Theoretically, macro-rupture of the model should occur at a water pressure of $p = \frac{1}{\alpha} f_t$ (f_t is the uniaxial tension strength of the rock).

As a quantitative evaluation of the pore pressure effect, the pore pressure and minimum effective principal stress distributions along the z-axis at the initial loading stage are shown in Fig. 4. It can be seen that the pore pressure distribution is completely uniform at both ends of the specimen. Although there is a correlation between the stress and pore pressure, the state of the stress field in the specimen is not entirely uniform, but statistically depends on the local heterogeneity in the mechanical properties of the specimen. Even though it is possible to calculate the relation between stress and strain up to the failure-point, the failure-point is not definitely predicted. No localized zone or fracture nucleation is observed before the macro-failure of the specimen, and thus, it is very difficult to predict where the nucleation will begin. A maximum fluctuation of $\sigma_{\min}^e$ that is 50% of the mean stress in the specimen is found. It is obvious that ignoring these stress fluctuations may result in incorrect conclusions if the fracturing process is conducted.

Figure 5(a) is the numerically simulated progressive failure process represented with elastic modulus. Correspondingly, the pore pressure evolution with the failure process is shown in Fig. 5(b). In the model that uses RFPA, the direction of the fracture growth is generally governed by the stress state and local damage evolution. Initially, the isolated "fractures" are located at "weak elements." Actually, in this stage, these isolated "fractures" should be called isolated failure elements. With the increased load, there is an increase in the appearance of isolated failure elements, which connect to each other to form macroscopic fractures. Due to the heterogeneity of the sample, a few randomly scattered elements first failed with the increasing hydraulic pressure. With the increase in applied water pressure, a primary tension fracture gradually comes into

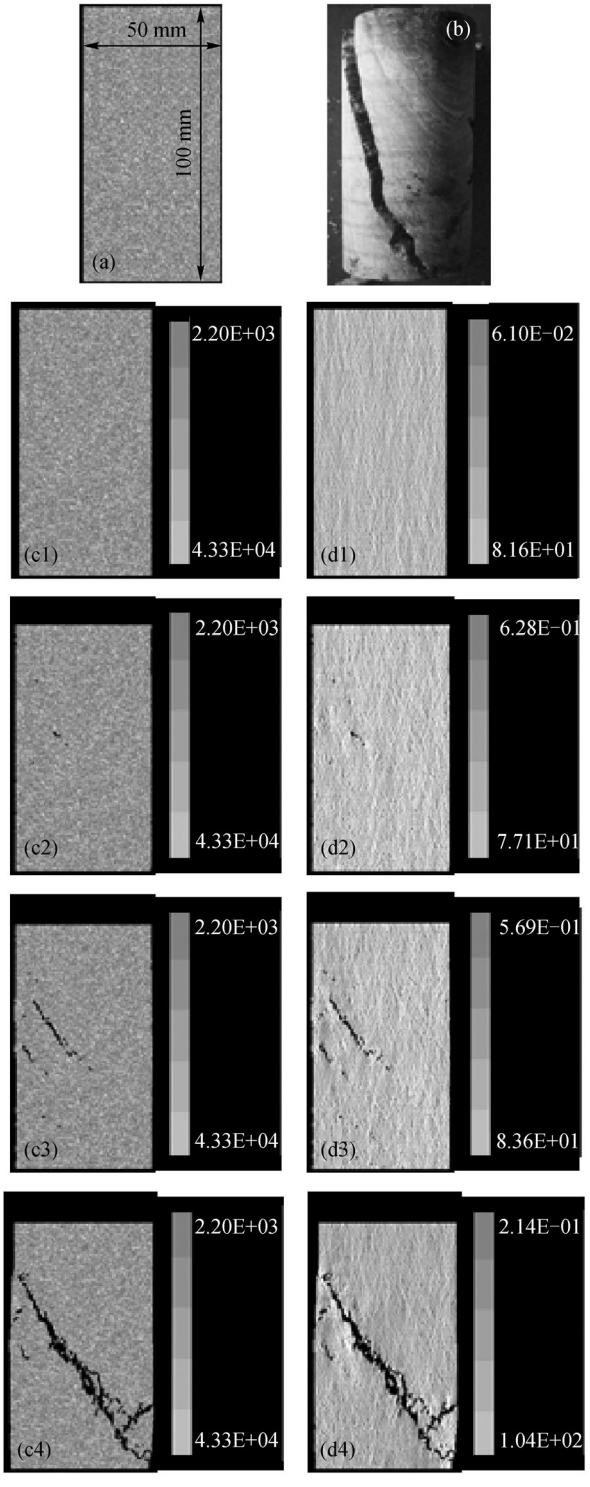

Fig. 2 Numerical calculation for the back analysis of the mechanical parameters, (a) model used for back analysis, (b) experimental laboratory result, (c) numerically obtained failure process, and (d) numerically obtained failure process (maximum shear stress evolution).

being perpendicularly to the *z*-axis of the specimen. It is interesting to note that the fracture growth path in the numerical simulation exhibits a jagged pattern, which is dependent on the element of the rock heterogeneity. The jagged fracture surface is a typical characteristic of tension failure (Renard et al., 2009; Haeri et al., 2014a, b; Yu et al., 2014) because a fracture will deterministically select a path of least resistance through the rock sample. When the

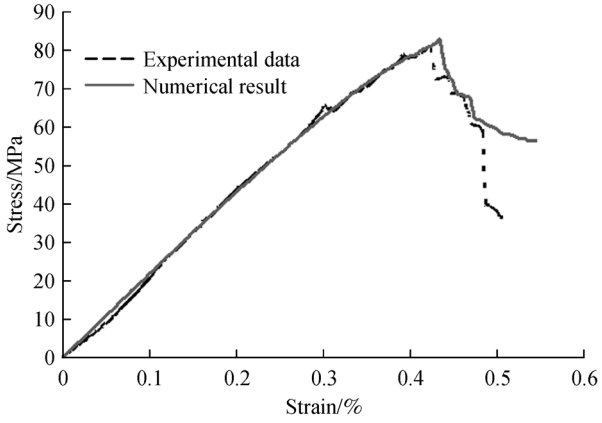

Fig. 3 The fitted stress-strain relationship.

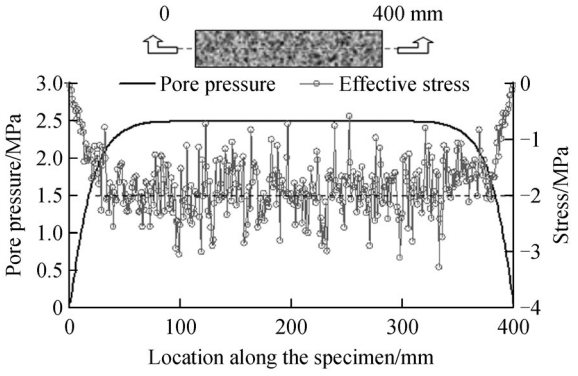

Fig. 4 Numerically obtained pore pressure and effective stress along the central line across the numerical specimen.

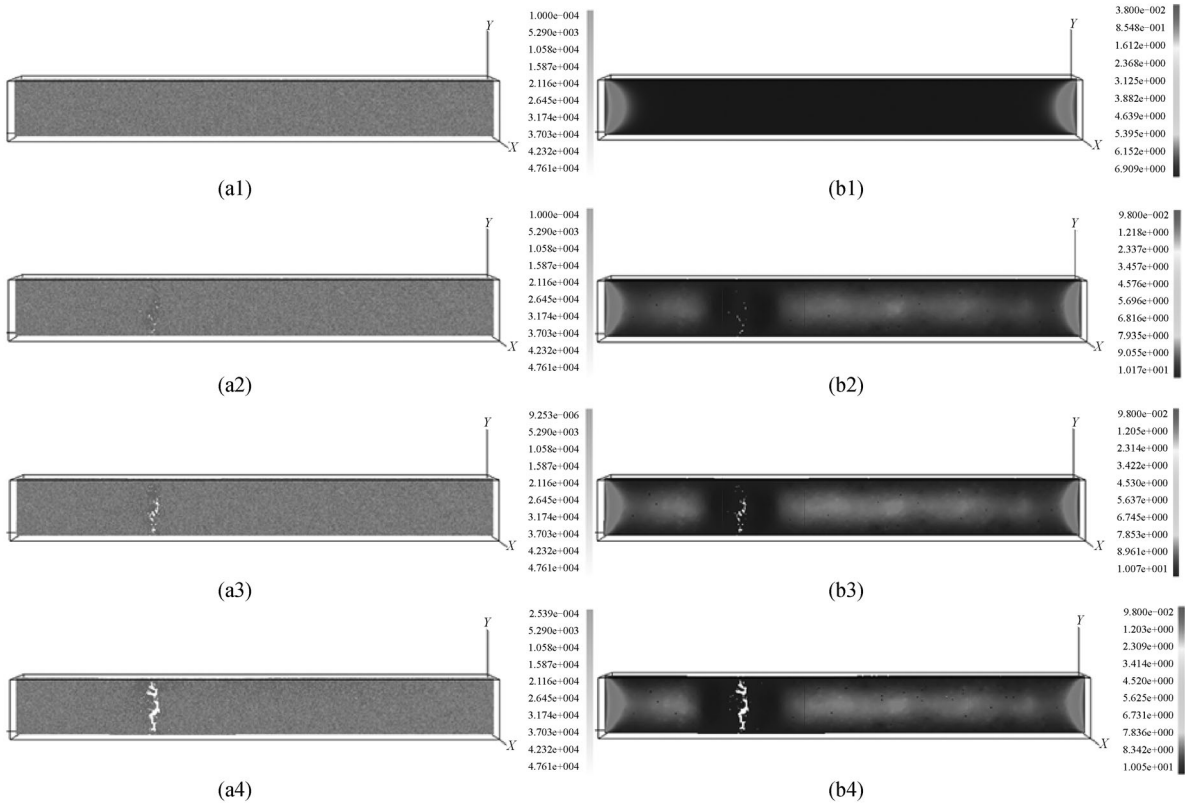

Fig. 5 Numerically obtained failure process of specimen under pure pore water pressure, (a) progressive failure process represented with elastic modulus, and (b) progressive failure process represented with pore pressure.

applied water pressure reaches approximately 10.2 MPa, the primary fracture penetrates the specimen causing it to rupture completely. The numerically obtained pressure at failure is consistent with that theoretically predicted above.

To compare the strength characteristic, a test with direct pull tension, but without the effect of pore pressure, was also numerically conducted using a specimen with the same dimensions and property parameters as those listed in Table 1. The specimen was extended along the horizontal direction (z-axis) until tensile fracture occurred. The stress-strain relationships for the specimen under direct pull tension are plotted in Fig. 6. The figure depicts the evolution of damage throughout the sample while subject to a constant strain rate. It is shown that the final tensile strength obtained in this direct pull simulation is 8.0 MPa. Based on the numerical results of pinch-off breaking and

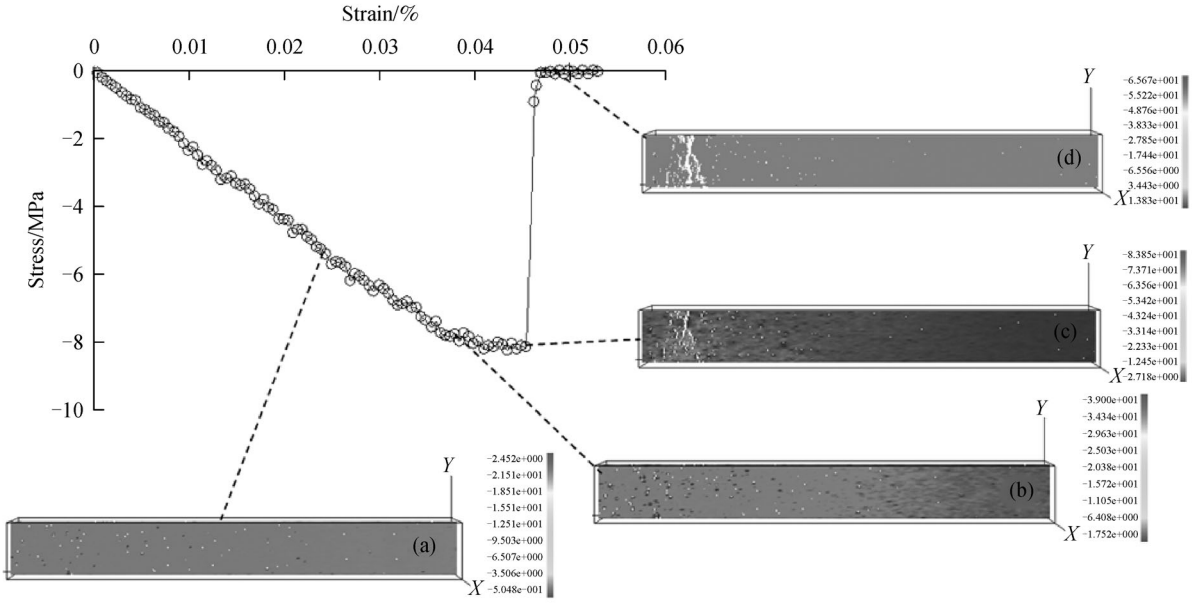

Fig. 6 Numerically simulated stress–strain curve and corresponding failure process for the case under direct pull tension.

the direct pull tension test, a pore pressure coefficient (α) of 0.784 is reversed and obtained, which agrees with the input value of 0.8 listed in Table 1. The pore pressure magnitude has a direct influence on tensile fracture initiation in rocks.

4 Numerical simulation of fracture growth within a non-uniform pore pressure field

The general direction of fluid flow due to pore pressure differences must also be considered (Jaeger and Cook, 1979; Bruno and Nakagawa, 1991; Boutt et al., 2009). For example, in one situation schematically shown in Fig. 7(a), fluid flows inwards toward an extending fracture tip. In the other situation, shown in Fig. 7(b), the fluid flow is directed outwards along a potential fracture path, such as along the line connecting two pressure sources. The induced forces are tensile and roughly perpendicular to the potential fracture path. When the far field stress state or internal crack loading is primarily tensile, the crack will conceptually extend along the x-axis, as shown in Fig. 8. Eq. (5) is the standard strain energy release rate for tensile fracture extension with the simple addition of the extra term αp.

$$G = \lim_{\Delta a \to 0} \frac{1}{2\Delta a} \int_0^{\Delta a} (\sigma_{yy} + \alpha p)(u_y^+ + u_y^-)\mathrm{d}x, \qquad (5)$$

where u_y^+ and u_y^- are the displacement components of the upper and lower fracture faces, respectively. This energy approach suggests that tensile fracture in a poroelastic body is directly dependent on the effective stress relation defined by Eq. (2). While the magnitude of pore pressure at the crack tip contributes directly to the strain energy release rate, the orientation of any pore pressure gradient field also influences the fracture extension. As described in Eq. (2),

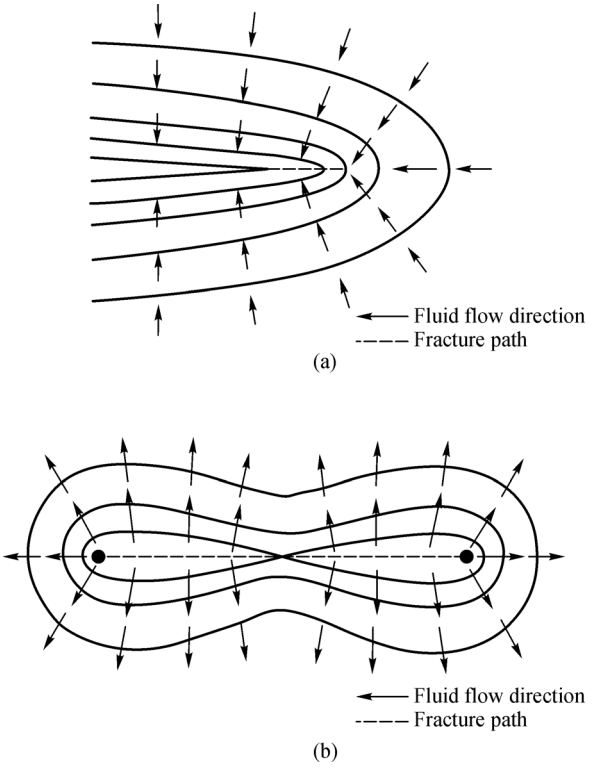

Fig. 7 The conceptual models of pore pressure gradient orientation affecting fracture extension, (a) fluid flow directed toward fracture extension, and (b) fluid flow directed away from potential fracture path (Bruno and Nakagawa, 1991).

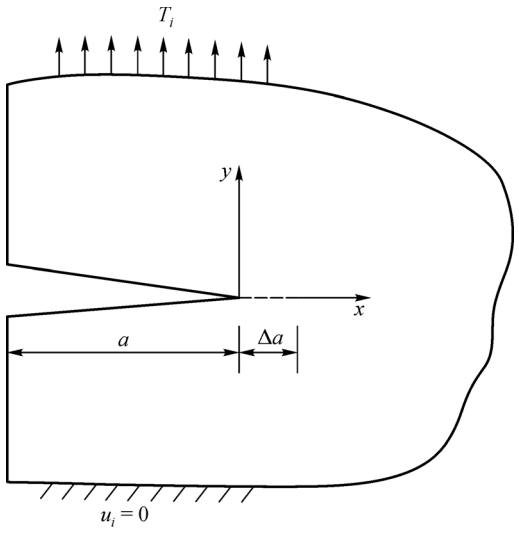

Fig. 8 The conceptual model of planar tensile fracture extension.

the pressure gradient term $-\alpha p$ enters the equilibrium equation for effective stresses on the rock matrix in the form of induced body forces. The pressure gradient field may either increase or decrease the effective stress, and hence, the strain energy release rate, depending on its direction with respect to the fracture.

In this section, a 2D double-notched specimen, as shown in Fig. 9, was employed. The model has been discretised into a 280 × 380 (106,400) mesh. We numerically extend this specimen in vertical direction under constant displacement control to investigate how the fluid flow will influence the growth of fractures initiated from the notches. Seven cases, listed in Table 2, are performed. The material parameters adopted in all cases are the same as those listed in Table 1.

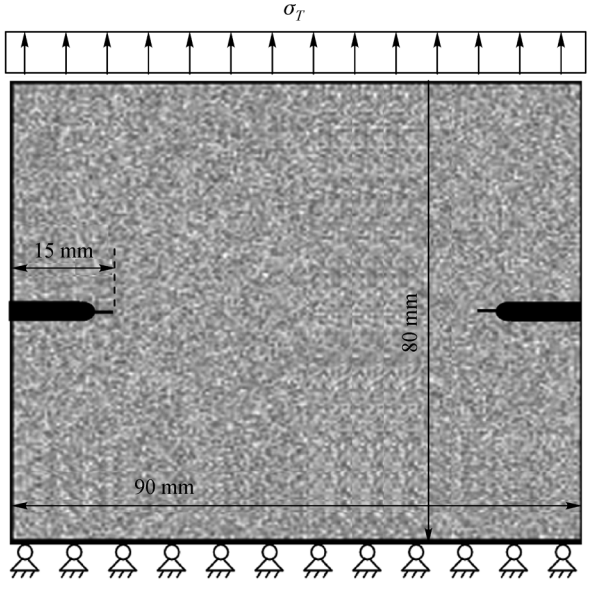

Fig. 9 The employed numerical model.

Table 2 Cases with different pore pressure applied on the left and right notches

Case	Magnitude of pore pressure applied on the left notch/MPa	Magnitude of pore pressure applied on the right notch/MPa
Case 1	0	0
Case 2	1	0
Case 3	2	0
Case 4	3	0
Case 5	1	1
Case 6	2	2
Case 7	3	3

To describe the numerical results in detail, Case 2, in which a water pressure of 1.0 MPa is applied in the left notch while keeping the right notch open to the atmosphere, is the focus of this section. Figure 10 shows the distribution of the pore pressure and the concentration of effective stress at the fracture tips at steady-state. Due to the applied water pressure in the notch, the concentrated tensile stress near the left notch tip is obviously higher than that near the right notch. The pore pressure gradient is used as a proxy for effective stress gradients; therefore, the stress manner suggests that it should be easier to initiate a fracture from the left notch tip.

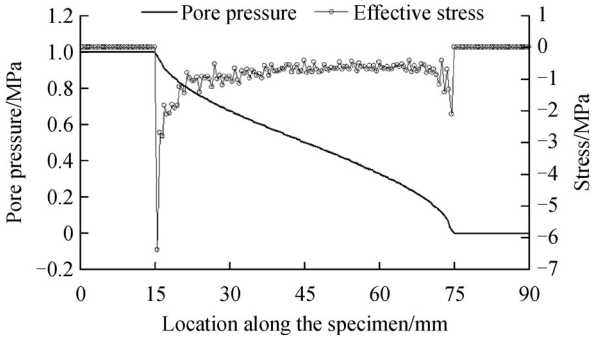

Fig. 10 Numerically obtained pore pressure and effective stress along the central line of the numerical specimen.

To study fracture growth, the four detailed figures in Fig. 11 present numerical results that represent pore pressure evolution and show the development of "rock bridging" in Case 2. The load–displacement curve is also plotted in Fig. 11 to indicate the loading stage that corresponds to the figure showing the failure process. As expected, the fracture is first initiated from the left notch and continues moving forward to the right side of the sample. Note that the fracture on the right later becomes inactive, whereas the fracture that started from the left becomes very active. Instead of growing directly, two other isolated fractures nucleate and grow in an overlapping manner. In Fig. 11(a)–

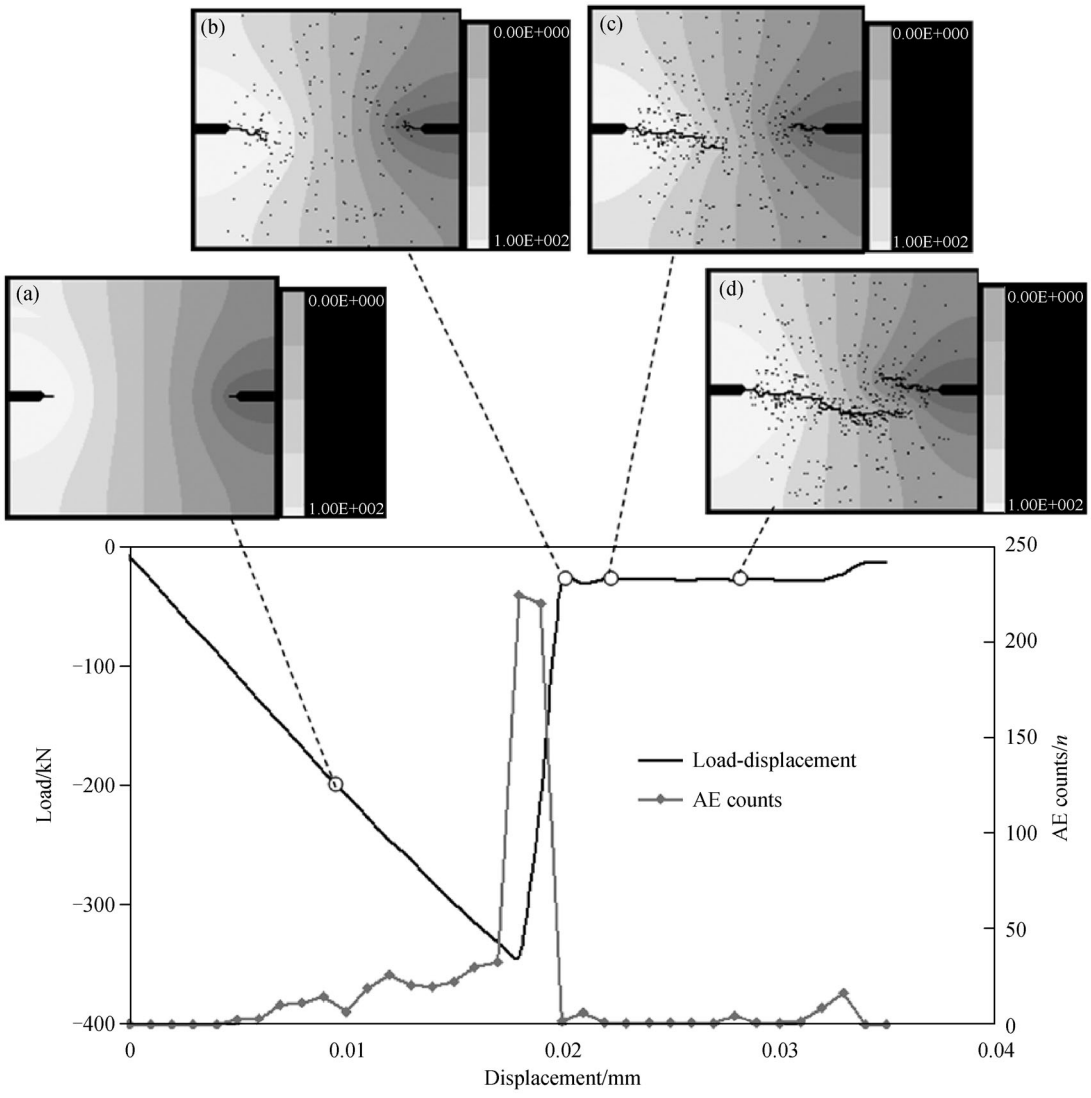

Fig. 11 Numerically simulated load–displacement curve and corresponding failure process for Case 2.

(d), it can be seen that the tip of the lower fracture has nearly reached the right notch, but the failure of the ligament (rock bridge) has still not occurred. As a result, stress can still be transferred through the ligament. The peak load for Case 2 is approximately 343 kN. Figure 11 (a)–(d) shows the pore pressure gradients at different stages. Initially, the higher pore pressure is mainly concentrated within the region adjacent to the left notch. Once a fracture is initiated, the evolution of the pore pressure is significantly affected by the fracture growth. Figure 11(c) shows that with fracture growth, the region with higher pore pressure gradually moved to the right, which further enhanced the non-symmetry of the pore pressure gradient. The profile of the primary fracture is characterized by numerous deflections, branching (bifurcating), and terminating. Although the deflection, branching, and terminating cost energy for fracture growth, the primary fracture initiated from the left notch eventually reaches the right notch along a flexural path of least resistance.

Figure 11 also shows the numerically obtained AE counts (event rates) as a function of vertical deformation for the numerical specimens. It is obvious that a large number of AE events occur before the peak load is reached. With increasing vertical extension displacement, an evident jump in AE counts occurs, which corresponds to the breakthrough of primary fractures and the drop of peak loads. The evident jump in AE counts and the decrease of peak loads reflect a strong brittle characteristic of the specimen; therefore, the increase of the vertical load is virtually linear until the peak load is reached.

The fluid flow in the rock surrounding the fracture when steady-state is reached is shown in Fig. 12. The water flowing mode is similar to that shown in Fig. 7, i.e., the

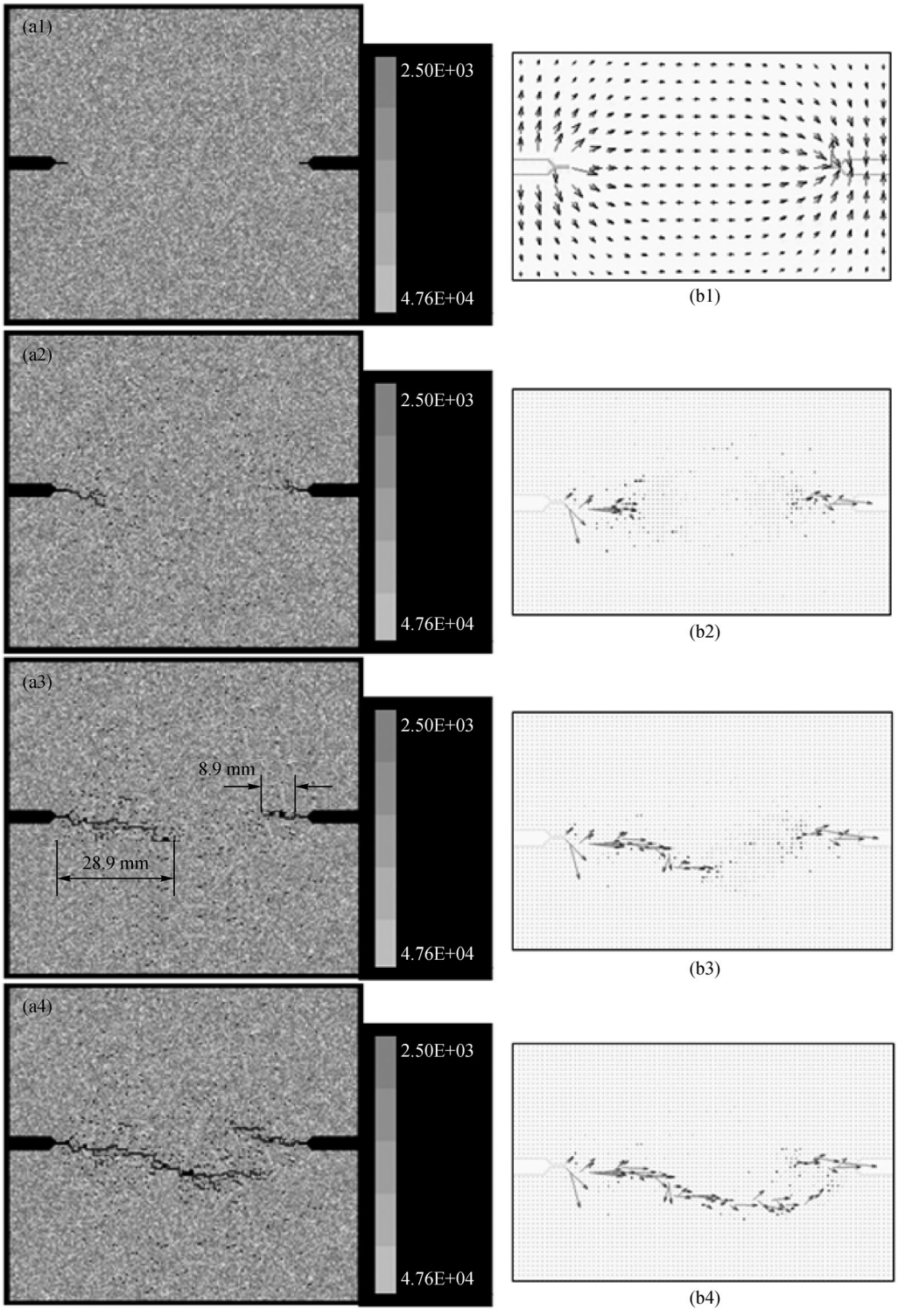

Fig. 12 Numerically obtained failure process of Case 2, (a) fracture growth process represented with elastic modulus, and (b) fracture growth represented with flow velocity.

water flows inward on the right side, toward the extending notch tip, while the water flow on the left side is directed outward along the notch tip. The numerical results reveal that the tortuous degree of the flow paths through the fractures in the failed specimen is dependent on the heterogeneity of the material. The fluid flows rapidly along

localized preferential flow paths through the newly formed fractures. As soon as the fractures nucleate, the fluid will by-pass the sample matrix and will then enter the fractures. Because the primary fractures are much larger than the micro-fractures in the matrix, the rate of infiltration into the primary fractures is greater than that in the matrix and micro-fractures (Fig. 12 (b4)).

Figure 13 shows the final failure mode for the first four cases. The overall fracturing patterns are similar to those in Fig. 12: the profiles of the hydraulic fracture are characterized by numerous deflections, branchings, and termination points. Although the general orientation of the fracturing path is perpendicular to that of the pull extension, the fracturing path on local scales is clearly dominated by the heterogeneity. The fracture lengths versus displacement for all cases are plotted in Fig. 14. It is shown that the more evident the non-uniformity of the pore pressure filled, the more asymmetric the left and right fracture lengths. Most noteably, the fractures initiated from the left notch are more active in Case 4 than those in the other cases, while the fractures initiated from the right notch are more clearly inhibited. The vertical load of Case 1, in which pore pressure effects were absent, is relatively lower than those of the other cases. This is because the fracture growth in Case 1 is symmetric, while the fracture growth in the other cases is asymmetrical due to the non-uniform pore pressure gradient. In the cases for asymmetrical pore pressure loading, the primary fracture initiated from the right notch stopped growing after extending a certain distance, whereas the primary fracture initiated from the left notch continued growing. The asymmetric growth requires greater force for the primary fracture to completely penetrate the central core of the specimen where the effective tensional stress is at its lowest.

To further investigate the influence of the pore pressure gradient on fracture growth, the fractured mode and corresponding fracture growth in the cases under an asymmetrical pore pressure gradient are illustrated in Figs. 15 and 16. The peak load of Case 1 is evidently higher than those cases with symmetric pore pressure loading. All these cases are under the combined conditions of vertical tensional stress and internal compressive pore pressure, causing the minimum principal effective stress to be less compressive and more tensile. Accordingly, a smaller vertical force is needed for the failure of these specimens, which indicates that the higher the magnitude of pore pressure applied on the notches, the faster the growth of the primary fractures, even though the growth of the fractures is symmetric in these cases.

The numerical results indicate that pore pressure effects must be considered at both local and global scales. While a local increase in pore pressure around the fracture tip may enhance fracture extension, a global increase in pore pressure may inhibit fracture growth by increasing the compressive in situ stresses in field.

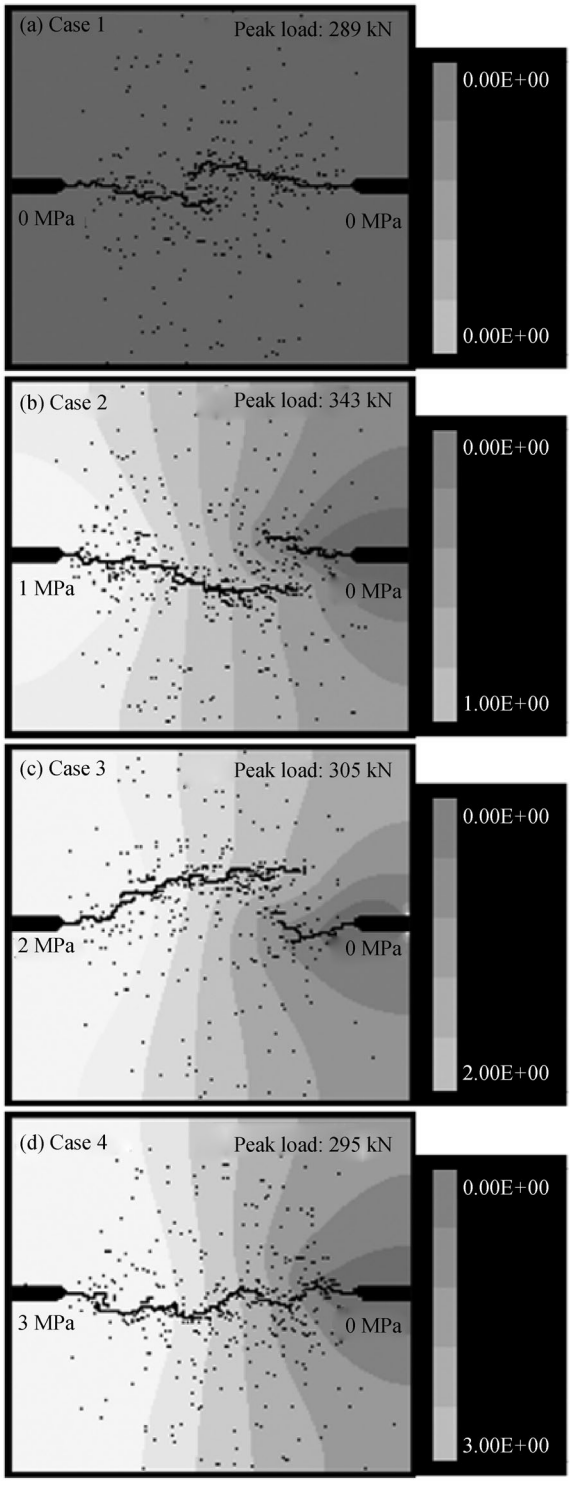

Fig. 13 Numerically obtained failure process for the cases under an asymmetrical pore pressure gradient (represented with pore pressure).

5 Conclusions

Although the reality is often much more complex than can be simulated by the applied numerical code, this study

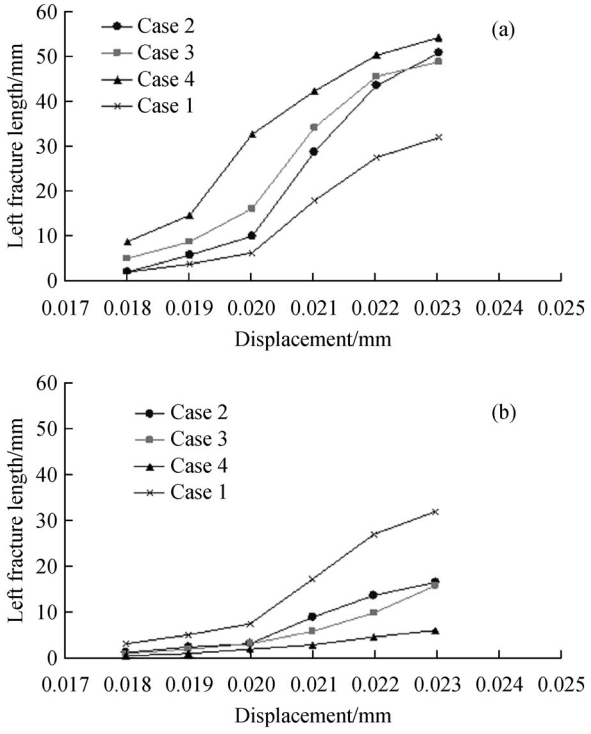

Fig. 14 The length variation of primary fractures initiated from the left and right notches with asymmetrical pore pressure, (a) left side, and (b) right side.

provides several interesting insights that lead to a better understanding of fracture growth associated with hydraulic fracturing. From the present numerical simulations, the following conclusions are derived.

In the tensile failure model, the effective stress analysis predicts a region in which the tensile strength of the rock is exceeded based on the stress distribution and the pore pressure. The simulation numerically confirmed and quantified that local pore pressure magnitude can directly contribute to the energy available for tensile fracture. The roughly straight path of the tensile fracture is reproduced by the numerical model, which is in agreement with the experimental results.

When the non-uniform pore pressure effect is considered, the numerically simulated results prove that the pore pressure gradient can influence the tensile fracture growth, which agrees with the theoretical prediction (Detournay et al., 1989; Bruno and Nakagawa, 1991; Berchenko and Detournay, 1997). When the fluid flows inwards toward an extending fracture tip, the pressure gradient field will inhibit the growth of fractures, yet it will accelerate the growth of fractures if the fluid flow is directed away from the potential fracture path. In addition, the numerical results show that the pore pressure gradient field can be modified with the growth of tensile fracture, i.e., the arrestment and/or acceleration of fractures will enhance the non-symmetry of the pore pressure gradient. The difference from the previous studies is that the permeability is not assumed to be infinite once the tensile criterion is satisfied. The tensile damage model predicts a region in

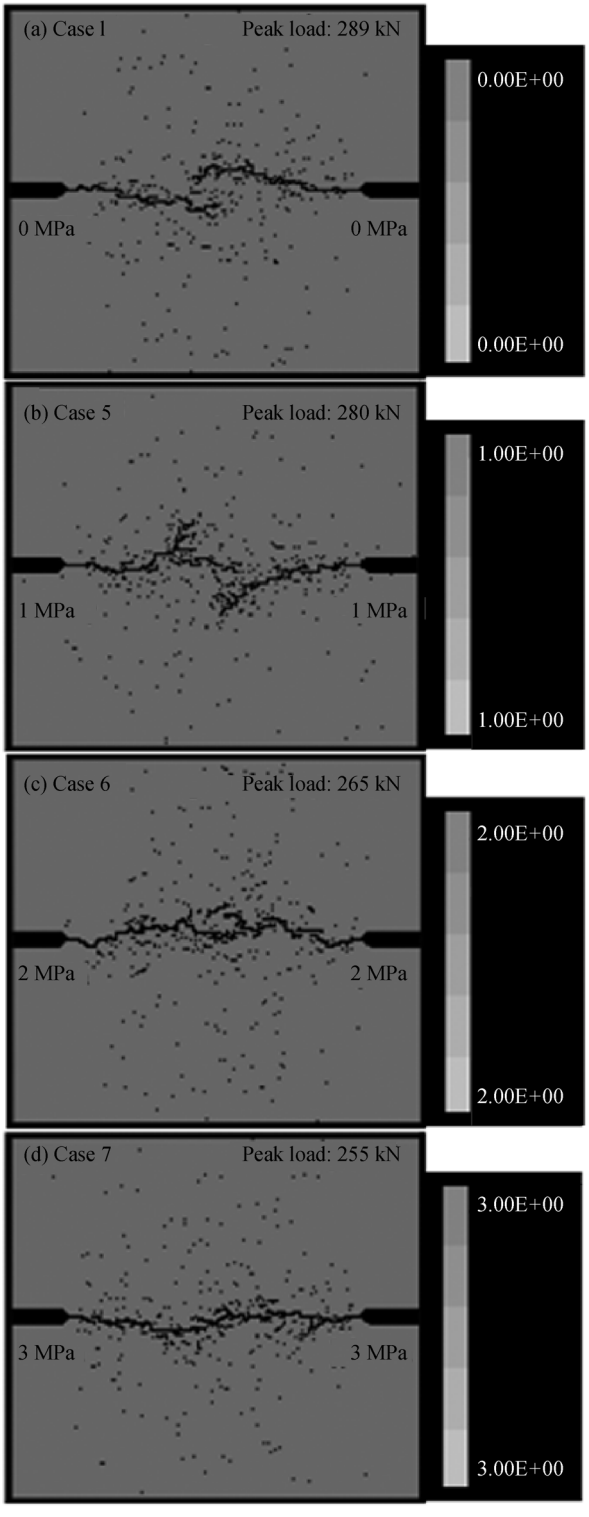

Fig. 15 Numerically obtained failure process for the cases under symmetric pore pressure gradient (represented with pore pressure).

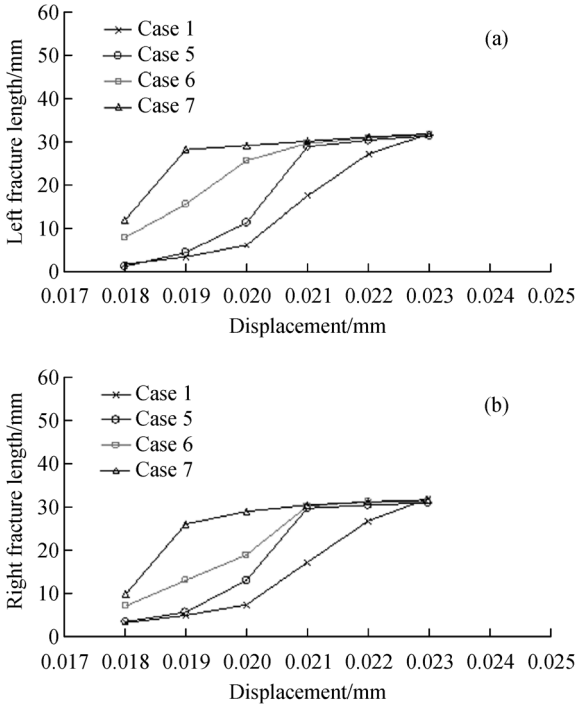

Fig. 16 The length variation of primary fractures initiated from the left and right notches with symmetric pore pressure, (a) left side, and (b) right side.

which tensile damage occurs, assigns a damaged permeability to this region, and calculates the change in apparent permeability of the rock.

The fracture initiation, growth, and coalescence; the breaking of intact rock; and the evolution of pore pressure in these stressed specimens are represented visually during the entire loading process. Deflection and branching are the most common fracture patterns, regardless of the magnitude and gradient distribution of the pore pressure. As a result, the fracturing path of the primary fracture is flexural. The failure modes are sensitive to the local disorder feature of the specimens, but the strength characterization of the specimens is more or less independent of this feature. The magnitude of pore pressure has a direct contribution to the ultimate bearing capacity of the rock samples. The numerical tests of the double-notched rock sample show that the greater the increase in pore pressure on the notches, the lower the ultimate tensile strength, which is consistent with the principle of effective stress in rocks.

Acknowledgements The study presented in this paper was jointly supported by grants from PetroChina Innovation Foundation (No. 2013D-5006-0211) and the National Natural Science Foundation of China (Grant No. 51479024). The authors are grateful for their support.

References

Abou-Sayed A S, Brechtel C E, Clifton R J (1978). In situ stress determination by hydrofracturing: a fracture mechanics approach. J Geophys Res, 83(B6): 2851–2862

Berchenko I, Detournay E (1997). Deviation of hydraulic fractures through poroelastic stress changes induced by fluid injection and pumping. Int J Rock Mech Min Sci Geomech Abstr, 34(6): 1009–1019

Biot M A (1941). General theory of three-dimensional consolidation. J Appl Phys, 12(2): 155–164

Blair S C, Cook N G W (1998). Analysis of compressive fracture in rock using statistical techniques: Part I. A non-linear rule-based model. Int J Rock Mech Min Sci, 35(7): 837–848

Boone T J, Wawrzynek P A, Ingraffea A R (1986). Simulation of the fracture process in rock with application to hydrofracturing. In J Rock Mech Min Sci, 23(3): 255–265

Boutt D F, Goodwin L, McPherson B J O L (2009). Role of permeability and storage in the initiation and propagation of natural hydraulic fractures. Water Resour Res, 45(5): W00C13

Bridgman P W (1912). Breaking tests under hydrostatic pressure and conditions of rupture. Philos Mag, 24(139): 63–80

Bruno M S, Nakagawa F M (1991). Pore pressure influence on tensile fracture propagation in sedimentary rock. Int J Rock Mech Min Sci, 28(4): 261–273

De Boer R, Lade P V (1997). The concept of effective stress for soil, concrete and rock. Geotechnique, 47(1): 61–78

Detournay E, Cheng A H D, Roegiers J C, McLennan J D (1989). Poroelasticity considerations in situ stress determination by hydraulic fracturing. Int J Rock Mech Min Sci Geomech Abstr, 26(6): 507–513

Griffith A A (1920). The phenomena of rupture and flow in solids. Phil Trans R Soc, A221: 163–198

Gudmundsson A, Kusumoto S, Simmenes T H, Philipp S L, Larsen B, Lotveit I F (2012). Effects of overpressure variations on fracture apertures and fluid transport. Tectonophysics, 581: 220–230

Haeri H, Shahriar K, Marji M F, Moarefvand P (2013). On the HDD analysis of micro cracks initiation, propagation and coalescence in brittle substances. Arabian Journal of Geosciences, doi: 10.1016/j.tecto.2012.05.003

Haeri H, Shahriar K, Marji M F, Moarefvand P (2014a). Experimental and numerical study of crack propagation and coalescence in pre-cracked rock-like disks. Int J Rock Mech Min Sci, 67: 20–28

Haeri H, Shahriar K, Marji M F, Moarefvand P (2014b). On the strength and crack propagation process of the pre-cracked rock-like specimens under uniaxial compression. Strength Mater, 46(1): 140–152

Holl A, Althaus E, Lempp C, Natau O (1997). The petrophysical behaviour of crustal rocks under the influence of fluids. Tectonophysics, 275(1–3): 253–260

Jaeger J C, Cook N G W (1963). Pinching-off and disking of rocks. J Geophys Res, 68: 1759–1765

Jaeger J C, Cook N G (1979). Fundamental of Rock Mechanics, 3rd Edn. London: Chapman & Hall

Jamveit B, Svensen H, Podladchikov J J, Planke S (2004). Hydrothermal vent complexes associated with sill intrusions in sedimentary basins. Geological Society of London, 234: 233–241

Kessels W, Kuck J (1995). Hydraulic communication in crystalline rock between the two boreholes of the continental deep drilling project in germany. Int J Rock Mech Min Sci Geomech Abstr, 32(1): 37–47

Li L C, Li S H, Tang C A (2014). Fracture spacing behavior in layered

rocks subjected to different driving forces: a numerical study based on fracture infilling process. Front Earth Sci, 8(4): 472–489

Li L C, Tang C A, Li G, Wang S Y (2012b). Numerical simulation of 3D hydraulic fracturing based on an improved flow-stress-damage model and a parallel FEM technique. Rock Mech Rock Eng, 45: 801–818

Li L C, Tang C A, Wang S Y (2012a). A numerical investigation of fracture infilling and spacing in layered rocks subjected to hydro-mechanical loading. Rock Mech Rock Eng, 45: 753–765

Li L C, Yang T H, Liang Z Z, Tang C A (2011). Numerical investigation of groundwater outbursts near faults in underground coal mines. Int J Coal Geol, 85(3): 276–288

Lin P, Huang B, Li Q B, Wang R K (2014b). Hazards and seismic reinforcement analysis for typical large dams following the Wenchuan earthquake. Eng Geol, doi: 10.1016/j.enggeo.2014.05.011

Lin P, Zhou W Y, Liu H Y (2014a). Experimental study on cracking, reinforcement and overall stability of the Xiaowan super-high arch dam. Rock Mech Rock Eng, doi: 10.1007/s00603-014-0593-x

Liu H Y, Kou S Q, Lindqvist P A, Tang C A (2004). Numerical studies on the failure process and associated microseismicity in rock under triaxial compression. Tectonophysics, 384(1–4): 149–174

Malvar L J, Fourney M E (1990). A three dimensional application of the smeared crack approach. Eng Fract Mech, 35(1–3): 251–260

McClintock F A, Argon A S (1966). Mechanical Behavior of Materials. MA: Addison-Wesley

Oliver N H S (2001). Linking of regional and local hydrothermal systems in the mid-crust by shearing and faulting. Tectonophysics, 335(1–2): 147–161

Pan P Z, Feng X T, Xu D P, Shen L F, Yang J B (2011). Modelling fluid flow through a single fracture with different contacts using cellular automata. Comput Geotech, 38(8): 959–969

Pan P Z, Rutqvist J, Feng X T, Yan F (2014). An approach for modeling rock discontinuous mechanical behavior under multiphase fluid flow conditions. Rock Mech Rock Eng, 47(2): 589–603

Pearce C J, Thavalingam A, Liao Z, Bicanic N (2000). Computational aspects of the discontinuous deformation analysis framework for modeling concrete fracture. Eng Fract Mech, 65(2–3): 283–298

Renard F, Bernard D, Desrues J, Ougier-Simonin A (2009). 3D imaging of fracture propagation using synchrotron X-ray microtomography. Earth Planet Sci Lett, 286(1–2): 285–291

Rozhko A Y, Podladchikov Y Y, Renard F (2007). Failure patterns caused by localized rise in pore-fluid overpressure and effective strength of rocks. Geophys Res Lett, 34(22): L22304

Rummel F (1987). Fracture mechanics approach to hydraulic fracturing stress measurements. In: Atkinson B, ed. Fracture Mechanics of Rock, New York: Academic Press, 317–239

Shimizu H, Murata S, Ishida T (2011). The distinct element analysis for hydraulic fracturing in hard rock considering fluid viscosity and particle size distribution. Int J Rock Mech Min Sci, 48(5): 712–727

Tang C A, Tham L G, Lee P K K, Yang T H, Li L C (2002). Coupled analysis of flow, stress and damage (FSD) in rock failure. Int J Rock Mech Min Sci, 39(4): 477–489

Terzaghi K (1943). Theoretical Soil Mechanics. New York: John Wiley and Sons

Wangen M (2011). Finite element modeling of hydraulic fracturing on a reservoir scale in 2D. J Petrol Sci Eng, 77(3–4): 274–285

Wang R, Kemeny JM (1994). Rock Mechanics. Rotterdam: Balkema

Weibull W (1951). A statistical distribution function of wide applicability. J Appl Mech, 18: 293–297

Wong T F, Wong R H C, Chau K T, Tang C A (2006). Microcrack statistics, Weibull distribution and micromechanical modeling of compressive failure in rock. Mech Mater, 38(7): 664–681

Wu K, Paton D, Zha M (2013). Unconformity structures controlling stratigraphic reservoirs in the north-west margin of Junggar basin, North-west China. Front Earth Sci, 7(1): 55–64

Yang T H, Tham L G, Tang C A, Liang Z Z, Tsui Y (2004). Influence of heterogeneity of mechanical properties on hydraulic fracturing in permeable rocks. Rock Mech Rock Eng, 37(4): 251–275

Yu J, Li H, Chen X, Cai Y, Mu K (2014). Experimental study of permeability and acoustic emission characteristics of sandstone during processes of unloading confining pressure and deformation. Chin J Rock Mech Eng, 33(1): 69–79

Yuan S C, Harrison J P (2005). Development of a hydro-mechanical local degradation approach and its application to modelling fluid flow during progressive fracturing of heterogeneous rocks. Int J Rock Mech Min Sci, 42(7–8): 961–984

Zhu W C, Liu J, Yang T H, Sheng J C, Elsworth D (2006). Effects of local rock heterogeneities on the hydromechanics of fractured rocks using a digital image-based technique. Int J Rock Mech Min Sci, 43 (8): 1182–1199

Zhu W C, Tang C A (2004). Micromechanical model for simulating the fracture process of rock. Rock Mech Rock Eng, 37(1): 25–56